



# Investigating the Impact of Friction Stir Processing on the Hydrogen Embrittlement in AA6082-T6 Heat-Treatable Aluminum Alloy

Ioannis G. Papantoniou<sup>1,2</sup> · Panagiotis Karmiris-Obratański<sup>1,3</sup> · Beata Leszczyńska-Madej<sup>4</sup> · Dimitrios E. Manolakos<sup>1</sup>

Received: 12 December 2023 / Accepted: 1 March 2024  
© The Author(s) 2024

## Abstract

This study investigates the impact of friction stir processing (FSP) on the hydrogen embrittlement (HE) in AA6082-T6 heat-treatable aluminum alloy. The effects of different number of FSP passes and different hydrogen cathodic charging (HCC) conditions on the material's response to HE are examined through comprehensive mechanical testing, microhardness analysis, and microstructural characterization. The results revealed that FSP leads to a decrease in yield strength, ultimate tensile strength, and microhardness, accompanied by an increase in energy absorption. The introduction of hydrogen through HCC significantly reduces mechanical properties, particularly in non-FSPed specimens. Notably, specimens with 8 FSP passes exhibit an interesting behavior with a slight increase in energy absorption and microhardness values after HCC. Microstructural analysis shows that FSP refines the microstructure, resulting in enhanced resistance to hydrogen-induced blistering effects. These findings contribute to the understanding of hydrogen embrittlement in FSPed aluminum alloys, providing insights for developing surface-modified materials suited for hydrogen-rich applications.

**Keywords** Friction Stir Processing · Hydrogen Embrittlement · Hydrogen Cathodic Charging · AA6082 · Fracture Analysis, Microstructure

## 1 Introduction

Friction Stir Processing (FSP) is a novel metalworking technique that leverages the fundamental principles of Friction Stir Welding (FSW) [1, 2]. It enables the local manipulation and control of microstructures within the near-surface layers of metallic components, leading to the creation of advanced microstructures and nanocomposite materials [3,

4]. The FSP process employs high temperatures and high strain rates to induce microstructural modifications, making it a versatile and eco-friendly solid-state fabrication method [5, 6]. In FSP, a cylindrical tool with a shoulder and a probe (pin) is employed to traverse the surface of the workpiece [7]. The tool's shoulder rubs against the surface, generating frictional heat that softens the material beneath [8]. The high strain rate of the revolving pin then deforms the softened material, leading to a change in its microstructure. The application of FSP is widespread across various industries, including automotive, energy, aerospace, aviation, and shipping [9–13].

FSP is a widely utilized method for enhancing various properties of parent materials, including microstructure [14, 15], mechanical properties [16–18], and corrosion resistance [19]. This is achieved through the production of ultra-fine grains, elimination of defects, breaking of dendrites, and regulation of the fraction of the secondary phase [20]. Extensive research has been conducted on the application of FSP, specifically in the context of aluminium alloys [21, 22]. Aluminium alloys are commonly used in various industries due to their attractive properties, such

✉ Ioannis G. Papantoniou  
ipapanto@central.ntua.gr

<sup>1</sup> School of Mechanical Engineering - Laboratory of Manufacturing Technology, National Technical University of Athens, Athens, Greece

<sup>2</sup> Department of Naval Architecture, School of Engineering, University of West Attica, Egaleo 12243, Greece

<sup>3</sup> Advanced Manufacturing Laboratory, Department of Manufacturing Systems, Faculty of Mechanical Engineering and Robotics, AGH University of Krakow, Krakow, Poland

<sup>4</sup> Department of Materials Science and Non-Ferrous Metals Engineering, Faculty of Non-Ferrous Metals, AGH University of Krakow, Krakow 30-059, Poland

as high strength-to-weight ratio, excellent corrosion resistance, and superior thermal and electrical conductivity [23, 24]. Sivanesh Prabhu et al. [25] investigated the friction and wear mechanism of AA6082/CaO<sub>3</sub> composite machined by the FSP method. The results show that the wear resistance mechanism of the FSP composite was two times increased compared to the FSP 6082 aluminium alloy. The mechanical, tribological and metallurgical properties of AA6061 composites containing B<sub>4</sub>C and Al<sub>2</sub>O<sub>3</sub> were investigated by Anandha Kumar et al. [26]. The wear studies showed that surfaces treated with FSP had better wear resistance compared to the base material when tested under dry sliding conditions, on the other hand on the worn surfaces they were observed microcracks and delamination. Mabuwa and Psomi [18] investigated the effects of multipass friction stir processing dissimilar AA6082 and AA8011 joints on fatigue. The results show fatigue life of joints between AA8011 and AA6082 was found to be improved with an increase in the number of FSP passes.

Hydrogen Embrittlement (HE) is a phenomenon that occurs in certain metals, including aluminum alloys, where hydrogen atoms are absorbed into the metal's lattice structure and cause degradation in its mechanical properties [27–29]. This degradation can result in decreased toughness [30], increased susceptibility to cracking [31], and ultimately, reduced reliability and safety of the metal component [32]. Aluminum alloys, depending on their composition and surface conditions, can absorb hydrogen when exposed to watery conditions, air saturated with water vapor, and water vapor combined with other gases such as nitrogen, argon, or dihydrogen (H<sub>2</sub>) [33]. The mechanisms that have been identified as major contributors to HE are the hydrogen-enhanced decohesion mechanism (HEDE), the adsorption-induced dislocation emission (AIDE), and the hydrogen-enhanced localized plasticity (HELP) [34, 35]. HEDE is a hydrogen embrittlement mechanism whereby hydrogen atoms infiltrate the metal lattice, resulting in the disruption of interatomic bonds. This leads to decohesion, or the separation of atoms, and subsequent propagation of cracks within the material. On the other hand, HELP is characterized by localized plastic deformation that is induced by the presence of hydrogen. This deformation results in strain localization, or the concentration of strain in specific regions, and the formation of micro voids [36]. A comprehensive understanding of these mechanisms is paramount in mitigating the detrimental effects of hydrogen-induced failures in engineering applications.

In the case of aluminium specimens, extensive research has demonstrated the significant influence of secondary phase (S-phase) particles on the corrosion behavior of the alloy, particularly in relation to grain boundaries [37]. Notably, S-phase particles such as Al<sub>7</sub>Cu<sub>2</sub>Fe and Al<sub>2</sub>CuMg

can induce galvanic corrosion and act as potent hydrogen traps [38]. By deliberately over-aging these alloys, it has been possible to control the microstructure adjacent to grain boundaries, resulting in a reduction in susceptibility to hydrogen embrittlement [39]. In an effort to explore the effect of oxidation films on hydrogen embrittlement susceptibility, Day and Chatteraj [40] conducted in-situ HE experiments on AA7075 using slow strain rates and two different aqueous media. The findings highlighted the significant role of the environment in the kinetics and formation of the oxidation film. Remarkably, the oxidation film exhibited a mitigating effect on HE at intermediate strain rates, whereas hydrogen embrittlement remained prominent at the slowest strain rates [41, 42].

Despite the widespread use of FSP to enhance and modify metallic alloys, limited attention has been given to study the susceptibility of FSPed specimens to hydrogen embrittlement. Up to now, only one research paper has investigated the effect of FSP on Hydrogen Embrittlement in aluminium alloys. More specifically, the study conducted by Papantoniou et al. [43] examined the impact of Friction Stir Processing on the hydrogen susceptibility of the work-hardened AA5083-H111 alloy through extensive mechanical and microstructural characterization. The results showed that the FSP process introduced a refined microstructure and enhanced the mechanical response of uncharged specimens. However, the introduction of hydrogen through intense hydrogen cathodic charging (HCC) led to surface defects, increased hydrogen diffusion, and degradation of mechanical properties, resulting in a more brittle mechanical response.

Therefore, the primary objective of this study is to advance our understanding of this phenomenon by investigating the influence of FSP on Hydrogen Embrittlement in heat-treatable aluminum alloys. Heat-treatable aluminum alloys can undergo material property changes induced by the FSP process (e.g. material softening due to dissolution of strengthening precipitates). Nevertheless, the potential advantages of FSP in mitigating hydrogen susceptibility, especially in the context of surface modifications through FSP, could offer significant benefits for components operating in hydrogen-rich environments. This study seeks to delve into these effects and assess the viability of using FSP as a means to improve the hydrogen resistance of aluminum alloys in practical applications. Furthermore, the knowledge gained from this study could prove valuable in comprehending the response of FSW welds to hydrogen-rich environments, contributing to a broader understanding of materials' behavior under such conditions. Specifically, we focused on AA6082-T6 in the current study. The alloy was subjected to hydrogen charging conditions to analyze the resulting microstructural changes, mechanical properties,

**Table 1** Chemical composition of AA 6082, wt%

Mg	Mn	Fe	Si	Cu	Zn	Cr	Ti	Al
0.9	0.7	0.5	1.0	0.1	0.1	0.2	0.11	Bal

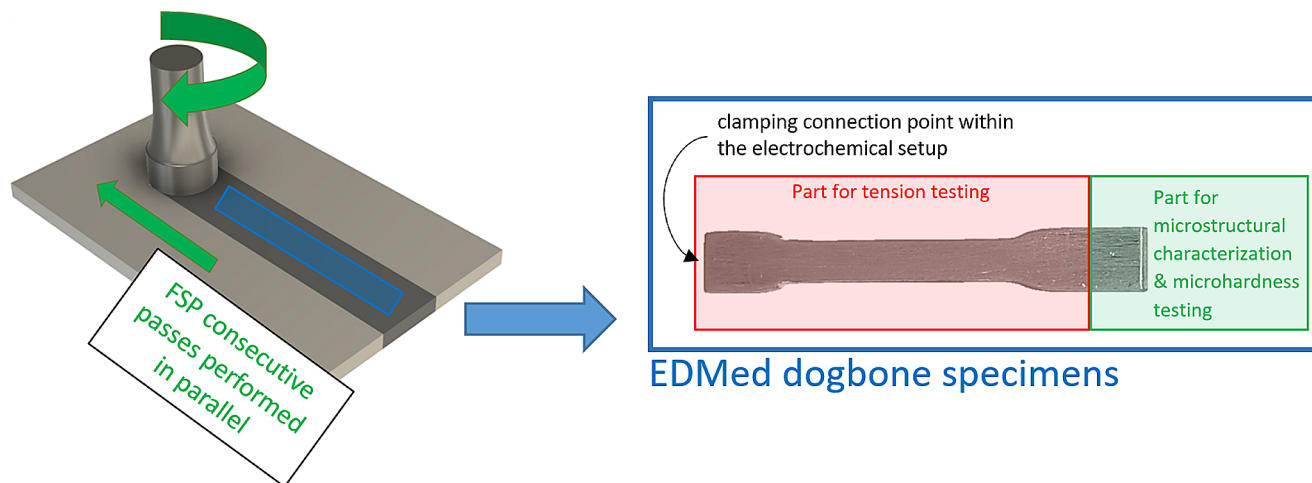


**Fig. 1** Schematic representation of the specimen preparation technique. The dogbone-shaped specimen was divided into two sections for different purposes. The left part of the specimen was utilized for

and potential degradation. Furthermore, FSPed specimens with varying numbers of passes underwent electrolytic HCC. While the typical approach involves using mild HCC parameters to minimize surface damage, this study employed intense charging conditions to examine how the refined microstructures respond to significant hydrogen-induced damage effects and simultaneous hydrogen diffusion. Both charged and uncharged specimens underwent tensile testing and microhardness evaluation analysis. The microstructure and fracture zone were examined using Optical Microscopy and Scanning Electron Microscopy (SEM).

## 2 Experimental Procedure

### 2.1 Materials

In the conducted experimental study, the FSP process was carried out using aluminum 6082 alloys in the T6 condition. This alloy belongs to the 6xxx series of aluminum alloys, which are classified as precipitation-hardening alloys. Its composition primarily consists of aluminum, with magnesium (Mg) and silicon (Si) serving as the key alloying elements. The typical chemical composition of AA6082 ranges from 0.7 to 1.3% Mg and 0.4%–1.0% Si. The addition of magnesium in the solid solution creates intermetallic structures during the heat treatment, enhancing the alloy's strength [44]. Due to its advantageous strength-to-weight ratio, AA6082 is widely used as structural components in the aerospace, automotive, and marine industries. This

mechanical testing, while the right part was dedicated to microstructural characterization and microhardness testing

particular alloy exhibits a tensile strength of up to 330 MPa, a yield strength ranging from 100 to 290 MPa, and a hardness between 80 and 120 HV. The following Table 1 contains the chemical composition of AA6082.

### 2.2 FSP & Specimen Preparation

The FSP experiments were conducted using a modified milling machine. Figure 1 provides a visual representation of the friction stir process employed. The FSP tool utilized in the experiments was manufactured from heat-treated tool steel. The tool had a flat shoulder with a diameter of 22 mm, while the pin had a cylindrical shape with a right-handed thread, measuring 4 mm in diameter and 5 mm in height. The operational parameters employed included a rotational speed ( $V_{rot}$ ) of 1000 rpm combined with a transverse speed ( $V_t$ ) of 70 mm/min. The parameters of rotational speed and traverse speed were chosen based on the optimum rotation-to-traverse speed ratio found in the literature for achieving optimal material mixing and joint strength during friction stir welding of AA6082 [45]. For the FSP passes, both 3 and 8 passes were performed in the same direction without allowing the samples to cool to room temperature between passes. The selection of these specific pass conditions was driven by the need to explore a range of operational parameters. The choice of three passes represents a more typical and practical scenario that might be employed in an industrial setting, balancing efficiency and cost-effectiveness. On the other hand, the use of eight FSP passes, although it may not be considered cost-effective in an industrial context,

was deliberate for this study. This intentional selection of eight passes aimed to investigate the impact of more intense operational parameters, providing valuable insights into the material's response under more rigorous conditions.

Following the completion of the FSP procedure, dogbone specimens were carefully prepared from the stir zone using Electro Discharge Machining (EDM) to ensure precise and representative samples. Significant attention was devoted to guarantee that the full gauge length of the specimens resided entirely within the stir zone, thereby capturing the complete effects of the FSP process on the material. Furthermore, an extra machining step was undertaken, involving the removal of a 2 mm layer from the upper surface of the dogbone specimens. This particular step served two crucial purposes. Firstly, it aimed to eliminate any surface irregularities or roughness that might have been introduced during the FSP operation, ensuring a clean and uniform specimen surface for subsequent testing and analysis. Secondly, it aimed to eliminate the "flow arm" region. The decision to exclude this region was driven by the understanding that the microstructure in this thin surface region is not significantly influenced by the FSP process and could potentially yield unexpected results during the hydrogen charging process. This approach ensured that the subsequent hydrogen embrittlement tests would focus on the most representative and relevant regions of the specimens, enhancing the reliability and accuracy of the experimental results.

The EDMed dogbone specimens exhibited a standardized geometry, with a length ( $L_c$ ) of 35 mm, a 6 mm width, and a 4 mm thickness. These dimensions were chosen in accordance with established testing standards and conventions, enabling direct comparisons and facilitating the accurate evaluation of mechanical properties. To ensure consistent and reproducible surface topography across all specimens, a multi-step grinding procedure was employed. Various SiC papers with progressively finer grit sizes were utilized, starting from coarser abrasives and gradually transitioning to finer ones. By following this grinding sequence, any surface imperfections or irregularities were progressively

reduced, leading to a uniform and controlled surface finish. Ultimately, finishing papers with a grit size of 2000 were employed to achieve a finely polished surface, characterized by a consistent and comparable surface topography across all dogbone specimens.

### 2.3 Hydrogen Cathodic Charging (HCC)

Hydrogen penetration into the dogbone specimens was achieved through the utilization of HCC. This technique employs electrolytic cathodic charging for the adsorption and diffusion process of hydrogen into the FSPed specimens (and the base material specimens). For this purpose, a solution containing 30 g/L NaCl and 3 g/L  $\text{NH}_4\text{SCN}$  electrolytes was employed.  $\text{NH}_4\text{SCN}$  inhibits the hydrogen recombination to  $\text{H}_2$  on the specimen surface to promote hydrogen uptake into the specimen. The duration of hydrogen charging was fixed at 8 h to ensure a sufficiently prolonged exposure for the adsorption and diffusion process of hydrogen into the FSPed specimens and the base material specimens. Two distinct charging current densities, namely 50 mA/cm<sup>2</sup> and 80 mA/cm<sup>2</sup>, were investigated. These current densities were deliberately chosen to provide considerably intense HCC charging conditions with respect to aluminum alloys. Although these conditions may be considered extreme, their implementation was deemed necessary to establish a clear correlation between the modified microstructures resulting from FSP and the subsequent effects of hydrogen diffusion and blistering. Furthermore, the selection of the applied current density and holding time was guided by the need to create intense hydrogen cathodic charging conditions that are relevant to potential real-world scenarios. Hydrogen blistering, in this context, refers to the formation of gas-filled blisters on the material's surface as a result of the interaction between hydrogen and the material [46]. These blisters can have a detrimental impact on the material's integrity and mechanical properties, making it an important factor to consider in this study. Detailed process parameters can be found in Table 2. Note that each set of specimens (e.g., B11) includes three specimens with the same parameters for charging current density, FSP passes, transverse speed, and rotational speed.

Upon completion of the hydrogen charging process, the specimens were carefully sectioned into two parts, as depicted in Fig. 1. The first part (dogbone shape) was specifically allocated for mechanical testing purposes, enabling the evaluation of the specimens' mechanical properties. Conversely, the second, smaller part was dedicated to comprehensive microstructural characterization and microhardness testing, facilitating a detailed examination of the specimens' microstructural features and hardness variations.

**Table 2** Process Parameters for Specimens

Test Series	charging current density (mA/cm <sup>2</sup> )	number of FSP passes	transverse speed (mm/min)	rotational speed (rpm)
B11	no charging	0	no FSP	no
B12	50	0		FSP
B13	80	0		
B21	no charging	3	70	1000
B22	50	3		
B23	80	3		
B31	no charging	8		
B32	50	8		
B33	80	8		

## 2.4 Microstructural Characterization

Microstructural characterization of the samples was conducted to investigate the changes in their microstructure before and after exposure to hydrogen embrittlement. This examination involved the utilization of an OLYMPUS GX51 light microscope and a Hitachi SU 70 scanning electron microscope, along with EDS analysis. Microphotographs were taken during operation of the secondary electron (SE) or backscattered electron (BSE) detector at an accelerating voltage of 10 and 15 kV. The EDS analysis enabled the identification and mapping of chemical elements within specific micro-areas, providing valuable insights into compositional variations induced by HE.

## 2.5 Mechanical Characterization

### 2.5.1 Tensile Testing

To minimize hydrogen loss, tensile testing experiments were conducted immediately after the hydrogen cathodic charging process following the ISO 6892 standard. The tests were carried out under ambient air conditions and at room temperature using a universal testing machine (Instron 4482) with a constant strain rate of  $7 \times 10^{-4} \text{ s}^{-1}$ . The data obtained from these experiments were used to generate stress-strain curves. From these curves, the values for energy absorption until failure, yield stress, and ultimate tensile strength (UTS) were calculated. Importantly, it should be noted that the values presented represent the mean derived from three independent experiments, ensuring the reliability and consistency of the results.

### 2.5.2 Microhardness Analysis

The microhardness distribution of the specimens was analyzed to gain insights into the material's response to hydrogen embrittlement. This analysis was performed to supplement the microstructural observations and correlate them with the results of the tensile tests. The microhardness characterization was conducted using an automated DuraScan 80 G5 microhardness tester manufactured by Struers. The testing followed the EN ISO 14577-1:2005 standard, with a total of 90 indentations made on each specimen using a load of 0.1 kgf. The indentations were arranged in a grid pattern with 4 rows, each containing 20 measurements. The spacing between each measurement was set at 0.1 mm. It is important to note that the microhardness of the 6082 alloy substrate was determined to be approximately 120 HV0.1, serving as a reference value for comparing and analyzing the observed microhardness distribution patterns in the tested specimens.

## 3 Results and Discussion

### 3.1 Mechanical Characterization

This section presents and analyzes the mechanical tensile testing results obtained in the study. The specimens were characterized based on the presence or absence of FSP and HCC, allowing for a comprehensive assessment of their mechanical properties. The energy absorption until failure, yield stress, and ultimate tensile strength were determined and compared across different specimen test series according to Table 2.

Figure 2 illustrates the stress-strain behavior for the different test sets where Fig. 3 presents plots illustrating the energy absorption, yield strength, and ultimate tensile strength values for a better evaluation of the results. Specifically, Fig. 3a-c highlight the effect of varying FSP passes under different charging conditions. These plots allow for a clear comparison and analysis of the relationship between FSP passes and the resulting energy absorption, yield strength, and UTS. On the other hand, Fig. 3d-e focus on the impact of charging conditions on specimens with different FSP passes (including the as-received material). These plots effectively showcase the effect of hydrogen cathodic charging on the energy absorption, yield strength, and UTS.

As for the materials without the introduction of hydrogen, Figs. 2 and 3b and c clearly demonstrate a significant decrease in the strength properties; both for the yield strength and the ultimate tensile strength of the material. This outcome was not unexpected and is consistent with the existing body of literature focused on the friction stir welding of precipitation-hardening alloys, including AA6082. AA6082 in the T6 condition is known to contain strengthening precipitates that contribute to its mechanical properties. The primary strengthening precipitate is  $\beta''\text{-Mg}_5\text{Si}_6$ , which remains stable at temperatures below 200 °C. However, the FSP process leads to the dissolution (and/or coarsening) of the hardening precipitates of the  $\beta''$  precipitates in the stir zone [39]. The dissolution can be attributed to a combination of factors including the elevated temperature (the process can exceed 200–250 °C), severe plastic deformation, and the consequential dynamic recrystallization phenomenon experienced by the material during the FSP process [47].

On the other hand, as seen in Fig. 3a, the dissolution of the strengthening precipitates led to a significant increase in of the energy absorption values. Interestingly, this increase is particularly pronounced in the specimen subjected to 3 FSP passes, while the specimen with 8 FSP passes exhibits a relatively lower increase. This contradicts the initial expectation that more FSP passes would result in greater material softening and consequently longer energy absorption

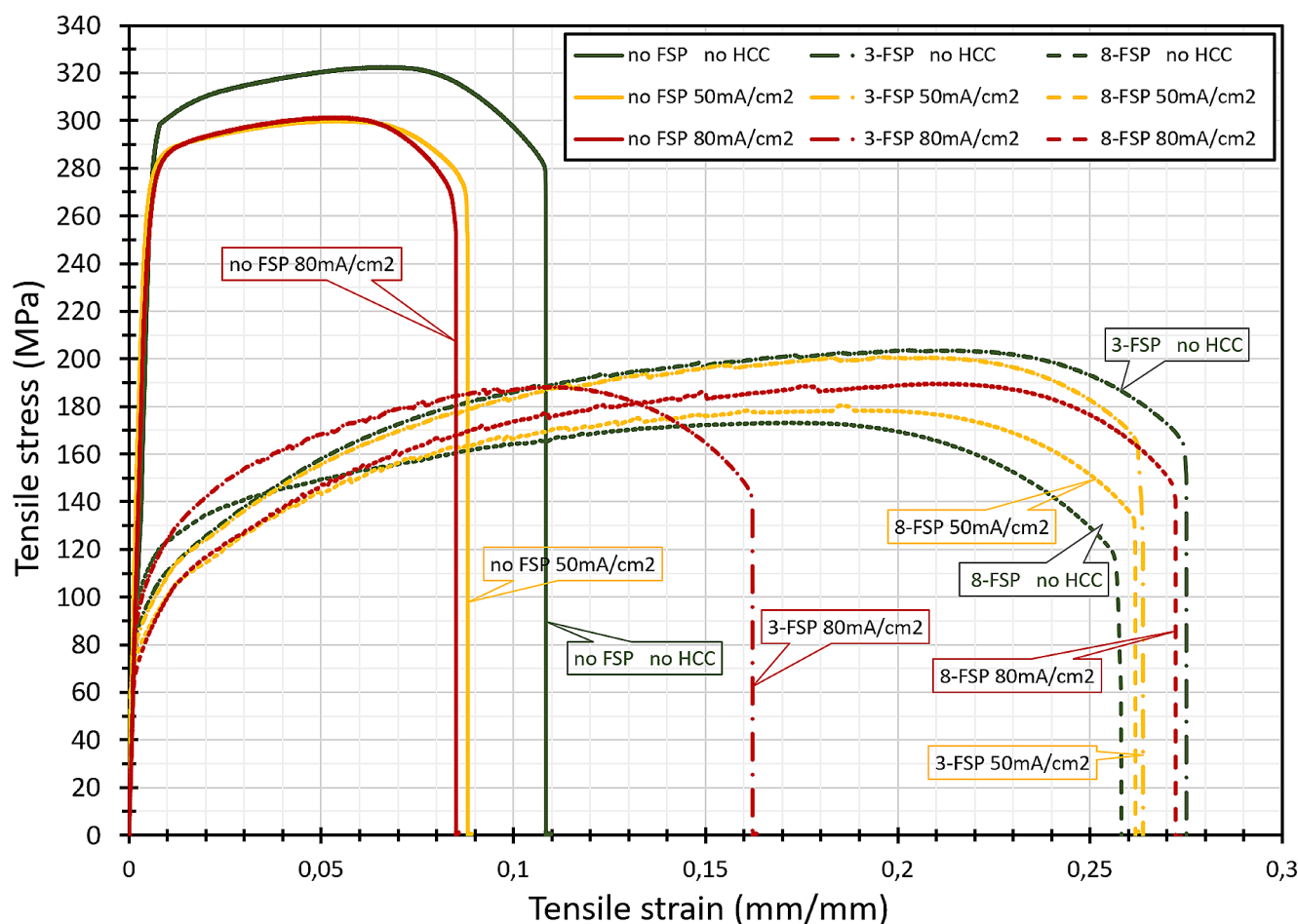


Fig. 2 Stress-strain diagrams obtained from tensile testing

values. Furthermore, it is noteworthy that the specimens with 8 FSP passes demonstrate a slight increase in the yield strength compared to those with 3 FSP passes, as indicated in Fig. 3b. This suggests that subsequent FSP passes may induce microstructural mechanisms that contribute to a slight strengthening effect in the material. This is in contrast with the logic that an increase in FSP passes inherently leads to continuous material softening. Instead, the observed trends suggest a more subtle relationship between FSP passes, microstructural changes, and resulting mechanical properties.

Upon analyzing Fig. 3d and e, and 3f, it becomes evident that the presence of hydrogen during hydrogen cathodic charging conditions resulted in a discernible alteration of the mechanical response of the specimens. Notably, for the non-FSPed specimens, HCC led to a significant reduction in the energy absorption, yield strength, and ultimate tensile strength. Interestingly, no substantial differences were observed between the two different charging current densities. For the specimens subjected to 3-FSP passes, a minor decrease in energy absorption was observed for the specimens charged at 50 mA/cm<sup>2</sup>, while a significant decrease

was observed for the specimens charged at 80 mA/cm<sup>2</sup>. However, no significant variations were noted in terms of yield strength and UTS between the charged and non-charged specimens.

The 8-pass FSPed specimens exhibited an unexpected response. The energy absorption and UTS values showed slight increases. This suggests that the diffusion of hydrogen into the material induced microstructural mechanisms that enhanced the mechanical response of the specimens. One possible explanation for this phenomenon could be an artificial aging effect caused by the HCC process or microstructural changes triggered by the diffused hydrogen. It is important to note that further research is required to fully understand the underlying mechanisms responsible for these observations. However, investigating this aspect falls outside the scope of the present paper.

### 3.2 Microstructural Characterization

The HCC process under intense charging conditions resulted in significant hydrogen induced blistering effects, leading to a reduction in thickness of the dogbone specimens. Figure 4

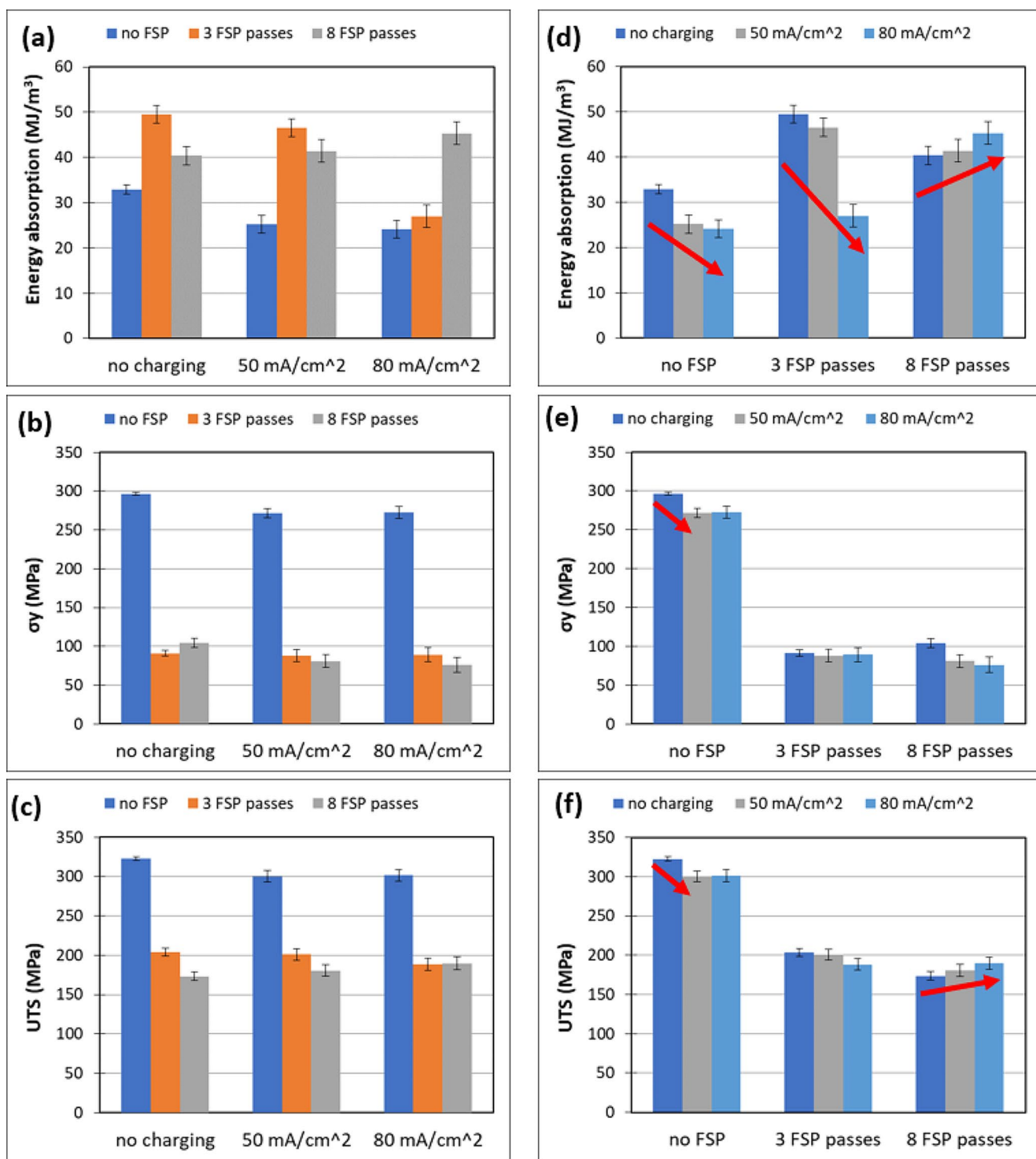
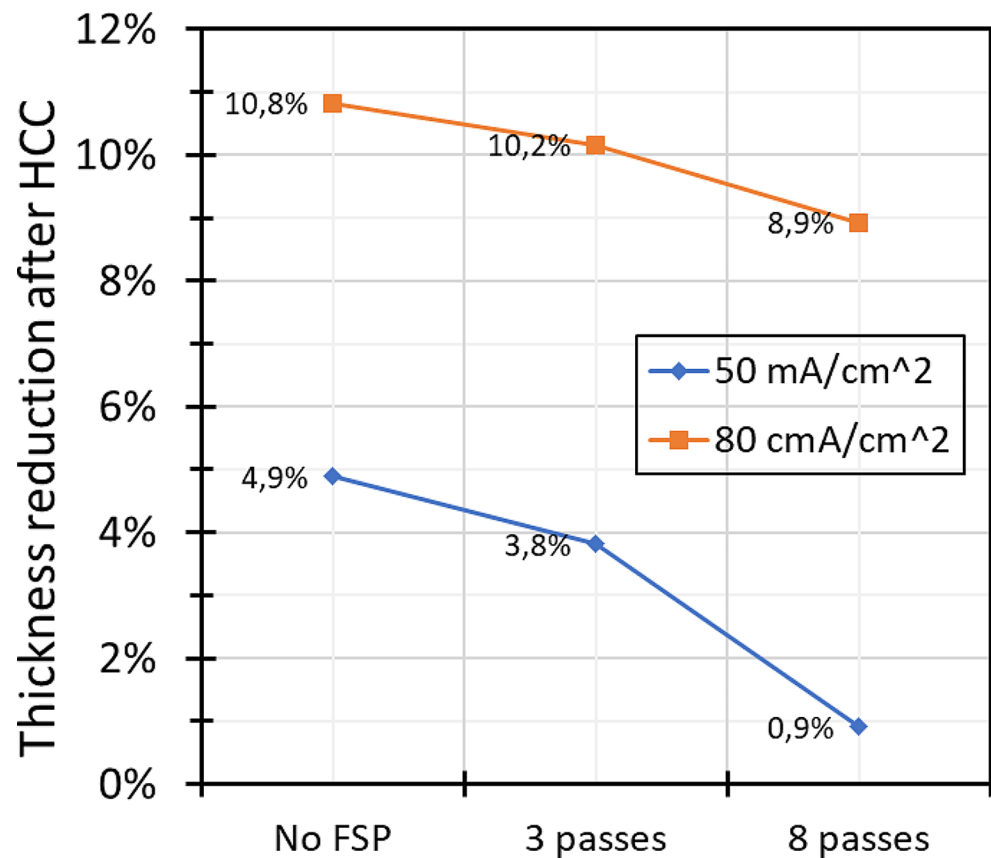


**Fig. 3** Impact of varying FSP passes in different charging conditions on (a) the yield strength, (b) the tensile energy absorption and (c) the UTS. The effect of different charging conditions on specimens with

varying FSP passes is shown for (d) the yield strength, (e) the tensile energy absorption and (f) the UTS.

**Fig. 4** Thickness reduction of dogbone specimens under HCC process



illustrates the extent of thickness reduction observed in all the charged specimens. It is evident that the specimens subjected to a charging current of 80 mA/cm<sup>2</sup> exhibited notably higher thickness reduction compared to those exposed to the lower current density of 50 mA/cm<sup>2</sup>.

Remarkably, the specimens treated with 3 and 8 FSP passes demonstrated reduced thickness reduction compared to the base material under both HCC current densities. This indicates that the refined microstructure achieved through FSP imparts enhanced resistance to hydrogen-induced blistering effects. Notably, the application of 8 FSP passes resulted in a significant reduction in blistering and thickness reduction, highlighting its effectiveness in mitigating these effects.

Figure 5 illustrates the near surface cross-sectional micrographs of specimens with and without the HCC process. Figure 5a and d, and 5g show the near surface microstructures of the as-received (without FSP surface treatment) specimen, and the specimens treated with 3 and 8 FSP passes, respectively. Notably, the FSPed specimens exhibited a significant refinement in the microstructure.

The base material specimens subjected to hydrogen charging displayed a notable surface profile characterized by significant roughness, attributed to the occurrence of intense blistering effects (Fig. 5b and c). In contrast, the specimens treated with 3 and 8 FSP passes exhibited a more

refined microstructure, resulting in significant smaller blisters and smoother surfaces and with a reduced waviness profile (Fig. 5e, f, h and i). The observed results regarding the surface profiles and blistering effects align with the findings on the thickness reduction of the dogbone specimens. The specimens treated with 3 and 8 FSP passes, which exhibited a more refined microstructure and reduced blistering, also displayed lower thickness reduction compared to the base material. These correlations suggest that the microstructural characteristics influenced the susceptibility to hydrogen-induced blistering, ultimately affecting the overall thickness reduction of the specimens.

Figure 6a, b and c displays the microstructure of the initial material (Fig. 6a) and the stir zone for specimens subjected to 3 and 8 FSP passes respectively (Fig. 6b and c). The FSPed specimens demonstrate a notable refinement in the microstructure compared to the base material. Table 3 provides further insights into the grain diameter values, revealing a reduction in average grain size from 92  $\mu\text{m}$  in the base material to 23  $\mu\text{m}$  after 3 FSP passes and 20  $\mu\text{m}$  after 8 FSP passes. Notably, there are no significant changes observed between the 3 and 8 FSP passes in terms of grain size. These findings highlight the effectiveness of FSP in achieving grain refinement, with the microstructure exhibiting a more uniform and refined nature. The changes in the microstructure during FSP can be attributed to various processes, including



**Fig. 5** Surface cross-section micrographs of specimens under different HCC conditions and FSP passes: (a) no FSP & no HCC (B11), (b) no FSP & 50 mA/cm<sup>2</sup> (B12), (c) no FSP & 80 mA/cm<sup>2</sup> (A13); (d) 3-FSP passes & no HCC (B21), (e) 3-FSP passes & 50 mA/cm<sup>2</sup> (B22), (f) 3-FSP passes & 80 mA/cm<sup>2</sup> (B23); (g) 8-FSP passes & no HCC (B31), (h) 8-FSP passes & 50 mA/cm<sup>2</sup> (B32), (i) 8-FSP passes & 80 mA/cm<sup>2</sup> (B33)

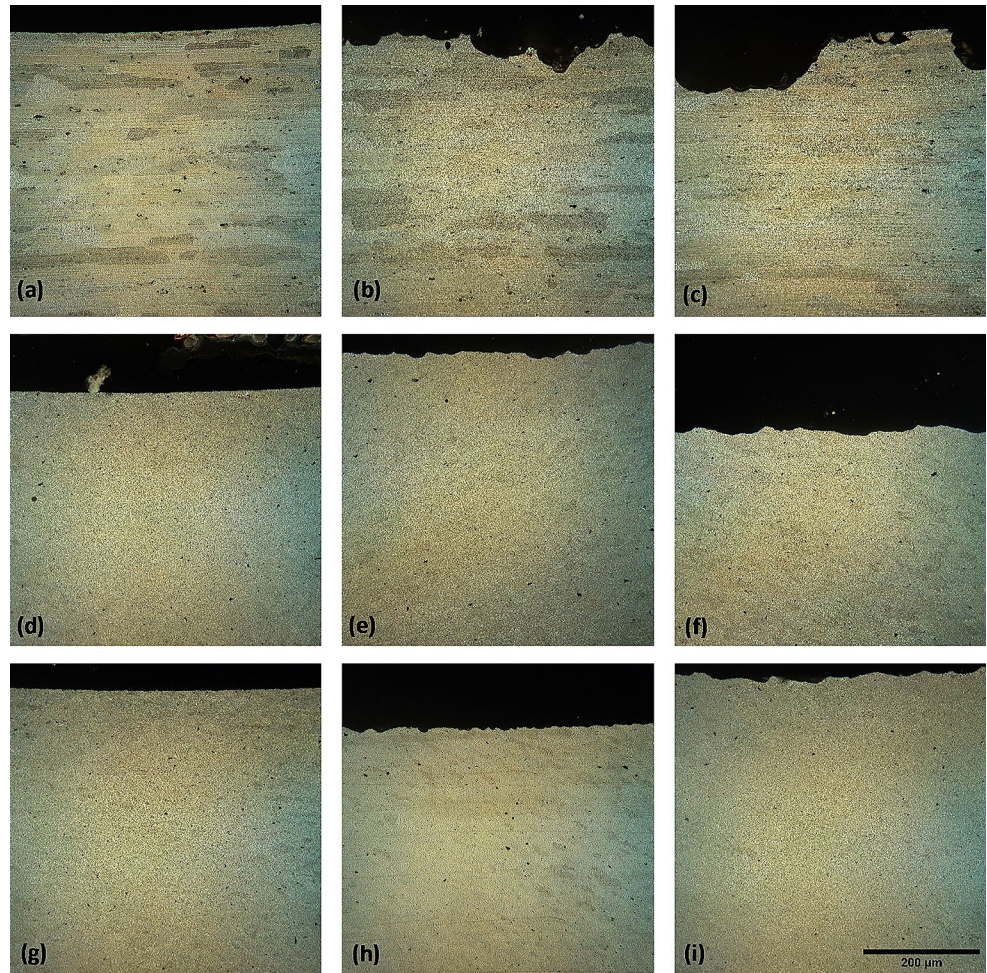


**Fig. 6** Microstructure of AA6082 sample in the: (a) initial state and after (b) 3 & (c) 8 FSP passes respectively

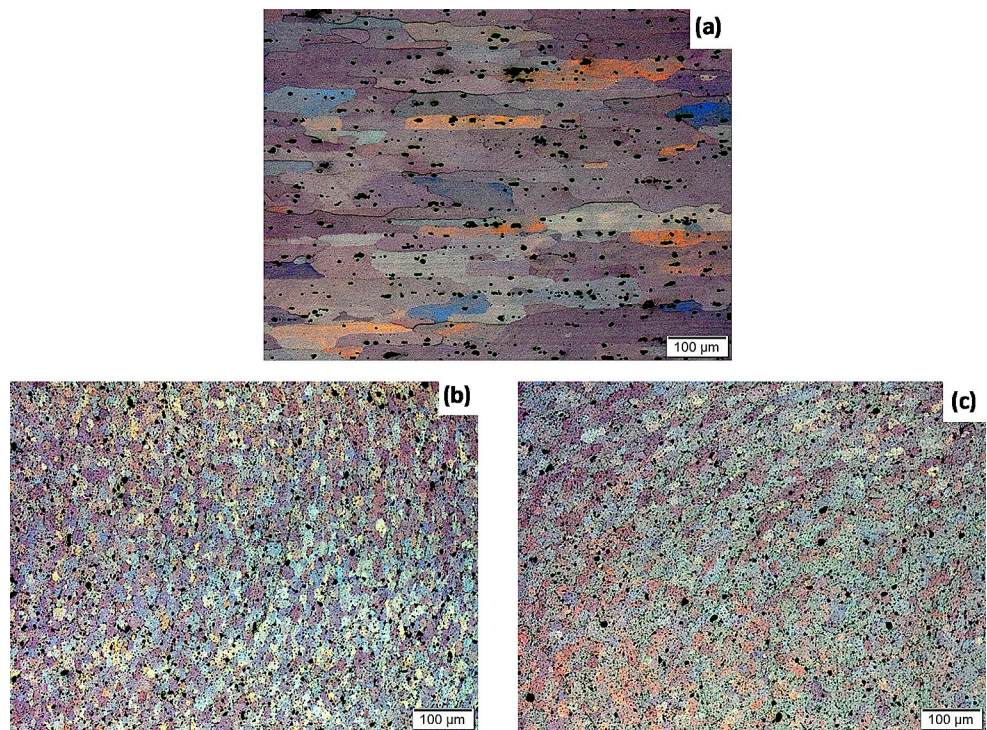


**Table 3** Average Grain Diameter before and after FSP

Sample	Average grain diameter, $d$ [ $\mu\text{m}$ ]	Minimum [ $\mu\text{m}$ ]	Maximum [ $\mu\text{m}$ ]
Base material	92	29	174
3 FSP	23	7.2	43
8 FSP	20	9.6	36

recrystallization (both static and dynamic), and refinement of second-phase particles. The material flow, temperature, and deformation gradient in the post-treatment zone contribute to homogenization refinement of the material.

Figure 7a and b showcase representative light microscopy images of 50 mA/cm<sup>2</sup> hydrogen-charged specimens, illustrating the base material and 8-pass FSPed specimens, respectively. These images were captured after polishing without chemical etching, allowing for clearer observation of large-scale hydrogen induced blistering mechanisms on the surface. The non-refined base material exhibits intergranular blistering extending to depths of approximately 200  $\mu\text{m}$ . In contrast, the refined microstructure of the 8-pass FSPed specimens displays intergranular blistering but with significantly reduced surface depths, reaching approximately 30  $\mu\text{m}$ . It is worth noting that the observed differences in blistering behavior suggest that the grain size plays a significant role in the susceptibility to hydrogen-induced damage, with the refined microstructure showing enhanced resistance to blistering compared to the non-refined base material.

Figure 8a and b depict scanning electron micrographs of the surface of the base material specimens at varying current charging densities (50 mA/cm<sup>2</sup> and 80 mA/cm<sup>2</sup>). In contrast, Fig. 8c and d showcase the corresponding surfaces of the 3-pass FSPed hydrogen charged specimens. A non-cohesive scale has formed on the surface of the specimens. In the case of the non-FSPed specimens, this scale covered the entire surface, as depicted in Fig. 8a and b. However, for the FSPed specimens, the scale was significantly smaller and only present in localized regions rather than uniformly across the entire surface, as illustrated in Fig. 8c and d. The reduced scale formation on the FSPed specimens correlates

with the lower thickness reduction observed after the HCC process.

The development of this scale is a consequence of the reaction between the test material and the corrosive environment. Detailed mapping analysis (Fig. 9) revealed that the scale primarily consists of elements present in the base material, including Al, Mg, Si, Mn, Fe, Ti, Cr, and Cu. Additionally, elements introduced from the electrolyte, such as C, O, Na, Cl, N, and S, were also detected within the scale.

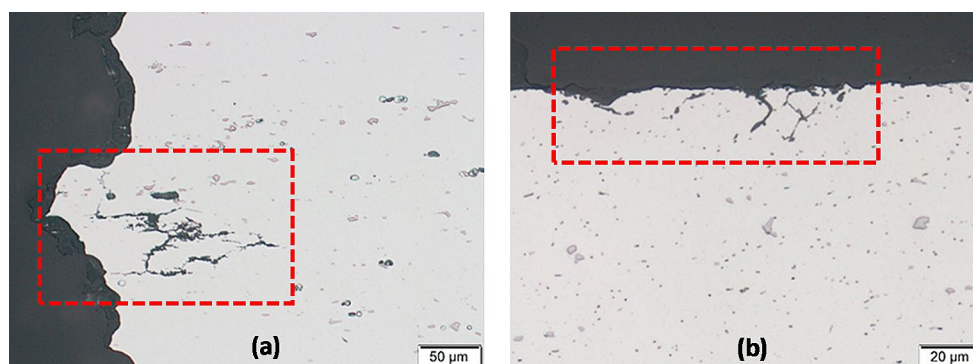
### 3.3 Microhardness Distribution Analysis

The microhardness measurements of the FSPed specimens and the base material (AA6082-T6) are presented in Fig. 10. The base material exhibited a scattered microhardness distribution with an average value of 120 HV [48, 49].

Based on the results (Fig. 10a), it was observed that the microhardness of the FSPed material exhibited a decrease compared to its initial value. This can be attributed to the plastic deformation and frictional heating during FSP that lead to the formation of a recrystallized equiaxed microstructure due to DRX phenomena. As a consequence of DRX, the resulting microstructure exhibits a low dislocation density. The softening observed in the specimen can also be ascribed to the decomposition of  $\beta''$  phase precipitates into Mg<sub>2</sub>Si ( $\beta$  phase) precipitates [50]. These precipitates play a crucial role in strengthening the material. The decomposition process leads to a reduction in the number and size of  $\beta''$  precipitates, resulting in a decrease in the strengthening effect and consequently contributing to the observed softening [51, 52]. Another reason that could lead to a decrease of the  $\beta''$  phase particles is the increased deformation that leads to redistribution of the second phase particles at the interior of the grains, causing softening [53].

The analysis of the HCC (Fig. 10b) in relation to the as-received alloy shows interesting findings regarding the microhardness of the samples. The microhardness is a measure of a material's resistance to indentation or penetration, and it is often correlated with its strength (yield strength and UTS). Upon considering the influence of HE, it is observed that there is a noticeable decrease in microhardness. This

**Fig. 7** Representative light microscopy micrographs of cross-sections of samples after HCC tests: (a) no FSP & 50 mA/cm<sup>2</sup> (B12), (b) 8-FSP passes & 50 mA/cm<sup>2</sup> (B32)



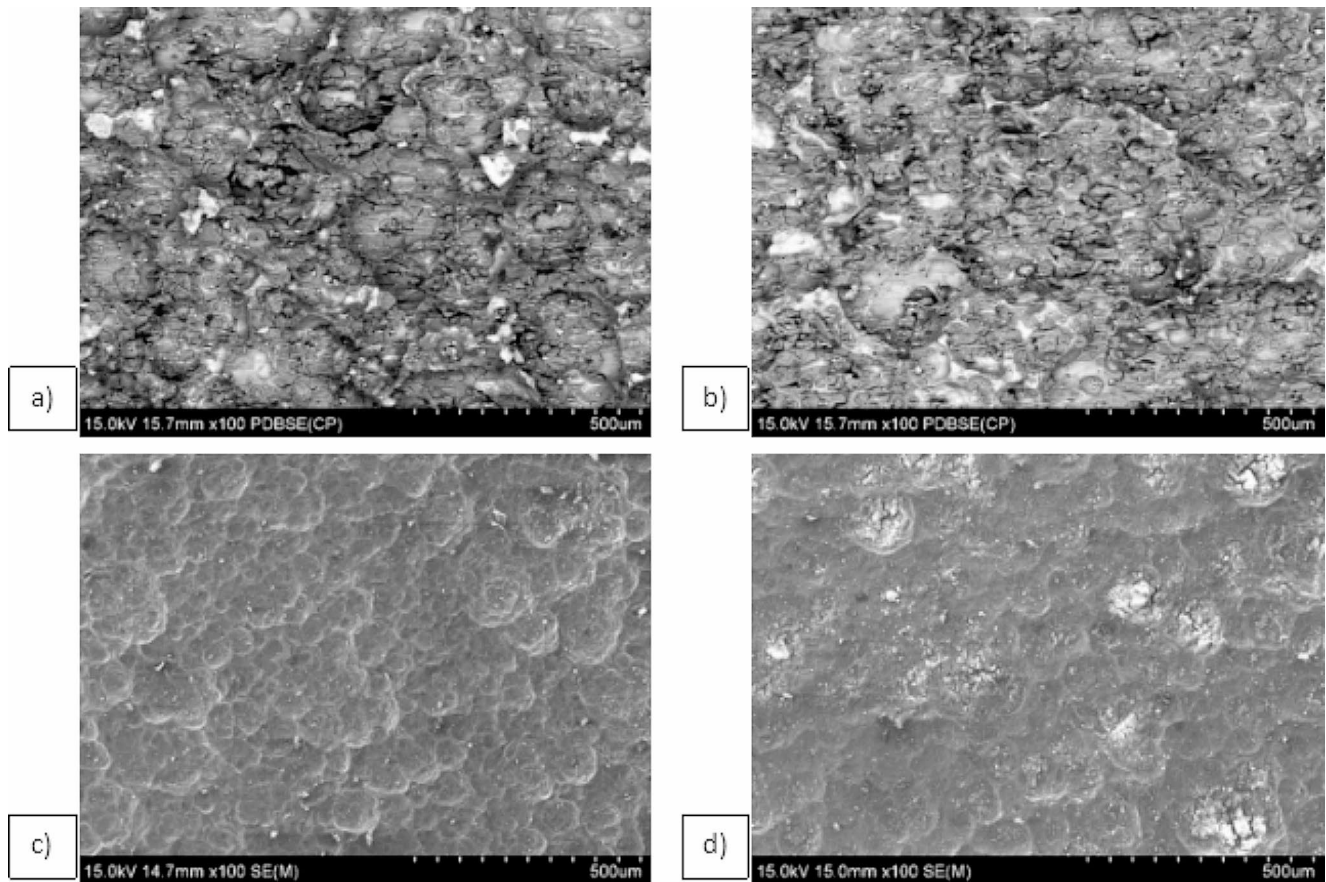


**Fig. 8** Scanning electron micrographs of surface morphology and scale formation of base material specimens and 3-pass FSPed specimens under HCC. (a) no FSP & 50 mA/cm<sup>2</sup> (B12), (b) no FSP &

80 mA/cm<sup>2</sup> (A13); (c) 3-FSP passes & 50 mA/cm<sup>2</sup> (B22), (d) 3-FSP passes & 80 mA/cm<sup>2</sup> (B23)

decrease can also be seen in the yield strength and UTS results (Fig. 3d&f), where a similar trend is observed with respect to different charging densities. Specifically, when comparing the as-received alloy to the HCC with a charging density of 50 mA/cm<sup>2</sup>, there is an average microhardness drop of 8.3%. This means that the microhardness value is 8.3% lower in the HCC sample compared to the as-received sample. Similarly, for the charging density of 80 mA/cm<sup>2</sup>, the average microhardness drop is 9.7%, corresponding to a microhardness value of 109.9HV<sub>01</sub> in the HCC sample.

For the specimens with 3 FSP passes that underwent hydrogen embrittlement (Fig. 10c), a similar response was observed, showing a reduction in surface hardness of approximately 8.8% for a current density of 50 mA/cm<sup>2</sup> and 11.7% for 80 mA/cm<sup>2</sup>. These reductions in hardness can be attributed to the effects of hydrogen embrittlement, which align with the findings from the tensile experiments (Figs. 2 and 3d, e and f).

In contrast, when analyzing the specimens subjected to 8 FSP passes, it becomes evident that the presence of hydrogen resulted in slightly higher microhardness profiles (Fig. 10d). A similar trend was observed for the ultimate

tensile strength and energy absorption (Fig. 3b and f). Consequently, the hydrogen cathodic charging process led to an increase in average depth microhardness of approximately 11.7% (from 68.3 to 79.3 HV<sub>01</sub>) for the 50 mA/cm<sup>2</sup> HE condition and 4% (from 68.3 to 73 HV<sub>01</sub>) for the 80 mA/cm<sup>2</sup> HE condition.

The decrease in hardness after HCC for the 3 FSP passes specimens can be attributed to the combined effects of hydrogen embrittlement and microstructural changes. During HCC, hydrogen atoms infiltrate the metal lattice and disrupt interatomic bonds, leading to reduced hardness. Additionally, the FSP process introduces heat and mechanical deformation, which can alter the microstructure. In the case of the 3 FSP passes specimens, the microstructure may have undergone recrystallization and the dissolution or coarsening of hardening precipitates, resulting in a softer material and a decrease in hardness. On the other hand, the observed increase in hardness (along with the UTS & energy absorption) after HCC for the 8 FSP passes specimens can be attributed to the unique combination of microstructural refinement and hydrogen embrittlement effects. The refined microstructure achieved through 8 FSP passes

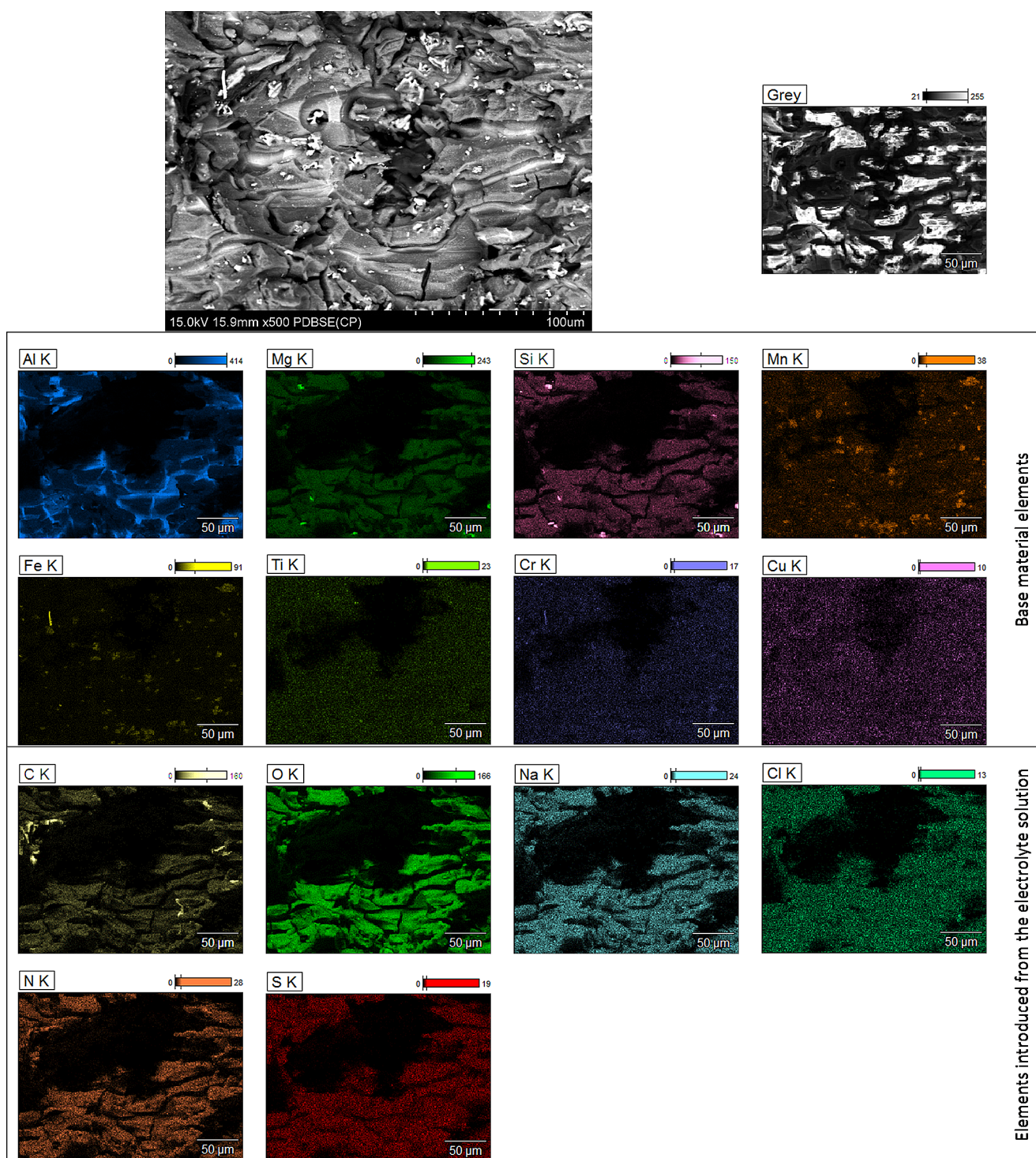


**Fig. 9** Elemental mapping analysis of the scale formed on the surface of the specimens under hydrogen cathodic charging. The scale primarily consists of elements present in the base material, including Al, Mg,

Si, Mn, Fe, Ti, Cr, and Cu. Additionally, elements introduced from the electrolyte, such as C, O, Na, Cl, N, and S, were also detected within the scale

creates a higher density of dislocations and vacancies, which can act as trapping sites for hydrogen atoms. The presence of hydrogen facilitates dislocation movement and plastic deformation, resulting in strain hardening and an increase in hardness. Additionally, the pinning effect of hydrogen on dislocations can contribute to the observed increase in hardness [54, 55].

In the case of the as-received specimens (Fig. 10b) and the 3-FSP passes specimens (Fig. 10c), the hardness profiles exhibit significant alterations extending throughout the entire thickness of the specimens, up to 2 mm from the surface. This suggests that hydrogen has penetrated throughout the entire material, affecting its hardness. On the other hand, for the 8-FSP passes specimens, the hardness profiles after 1 mm from the surface appear similar between the charged and uncharged specimens. This indicates that the FSP process may have introduced microstructural modifications that mitigate the influence of hydrogen embrittlement on the material's hardness at greater depths.

### 3.4 Fracture Analysis

Figure 11 displays SEM micrographs of the fractured surfaces of specimens subjected to different conditions (FSP and HCC). The non-FSPed specimens exhibit a mixed-mode fracture with the presence of the features of the brittle and ductile fracture. The presence of large dimples indicates localized plastic deformation, suggesting a ductile fracture behavior characterized by stretching and tearing of the material [56]. The shear mechanism of fracture was active in the matrix, evident from the presence of oval dimples, suggesting a complex fracture pattern. The region

delineated by yellow dashed lines in Fig. 12 indicates the potential presence of intermetallic particles, which, due to their inherent brittleness, might serve as initiation sites for crack propagation, leading to void formation in these areas. Notably, despite different charging conditions, no significant variations are observed in these fracture characteristics.

On the other hand, the FSPed specimens show a typical ductile failure mode, where the fractured surfaces display significant small dimples. The FSPed specimens with a higher number of FSP passes exhibit slightly smaller dimples compared to those with fewer passes. Locally, particles of intermetallic phases are visible in the area of the dimples, but they are much finer than in the base material especially in the material after 8 passes of FSP.

Overall, the observations suggest that the FSPed specimens predominantly exhibit a ductile fracture behavior, characterized by the presence of small dimples. In contrast, the non-FSPed specimens display a mixed-mode fracture with both ductile and brittle features in the regions of the small particles of the intermetallic phase occurrence. These findings align with the results obtained from tensile testing, further supporting the correlation between the fracture behavior and mechanical properties of the specimens.

## 4 Conclusions

This study investigated the mechanical and microstructural characteristics of the heat-treatable aluminum alloy 6082 (in T6 condition) under different conditions of friction stir processing and hydrogen cathodic charging. The following conclusions can be drawn from the results:

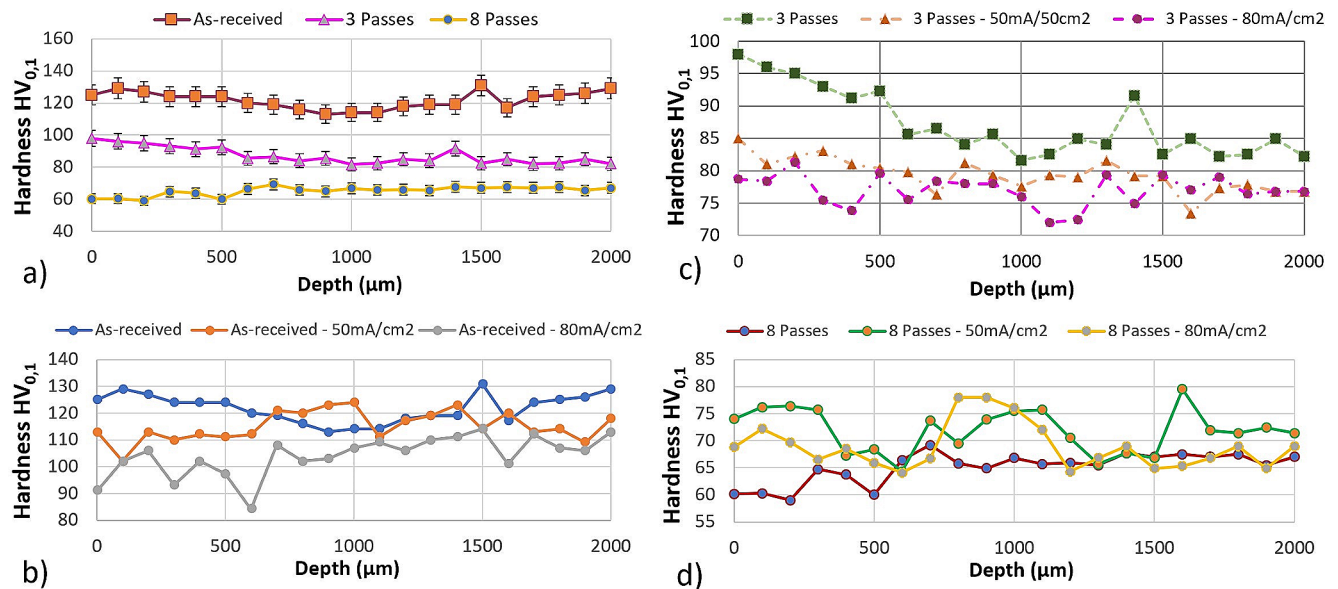


**Fig. 10** Microhardness depth analysis for: (a) no HCC: as-received, 3 FSP, 8 FSP; (b) as-received: no HCC, 50 mA/cm<sup>2</sup>, 80 mA/cm<sup>2</sup>; (c) 3 FSP: no HCC, 50 mA/cm<sup>2</sup>, 80 mA/cm<sup>2</sup>; (d) 8 FSP: no HCC, 50 mA/cm<sup>2</sup>, 80 mA/cm<sup>2</sup>

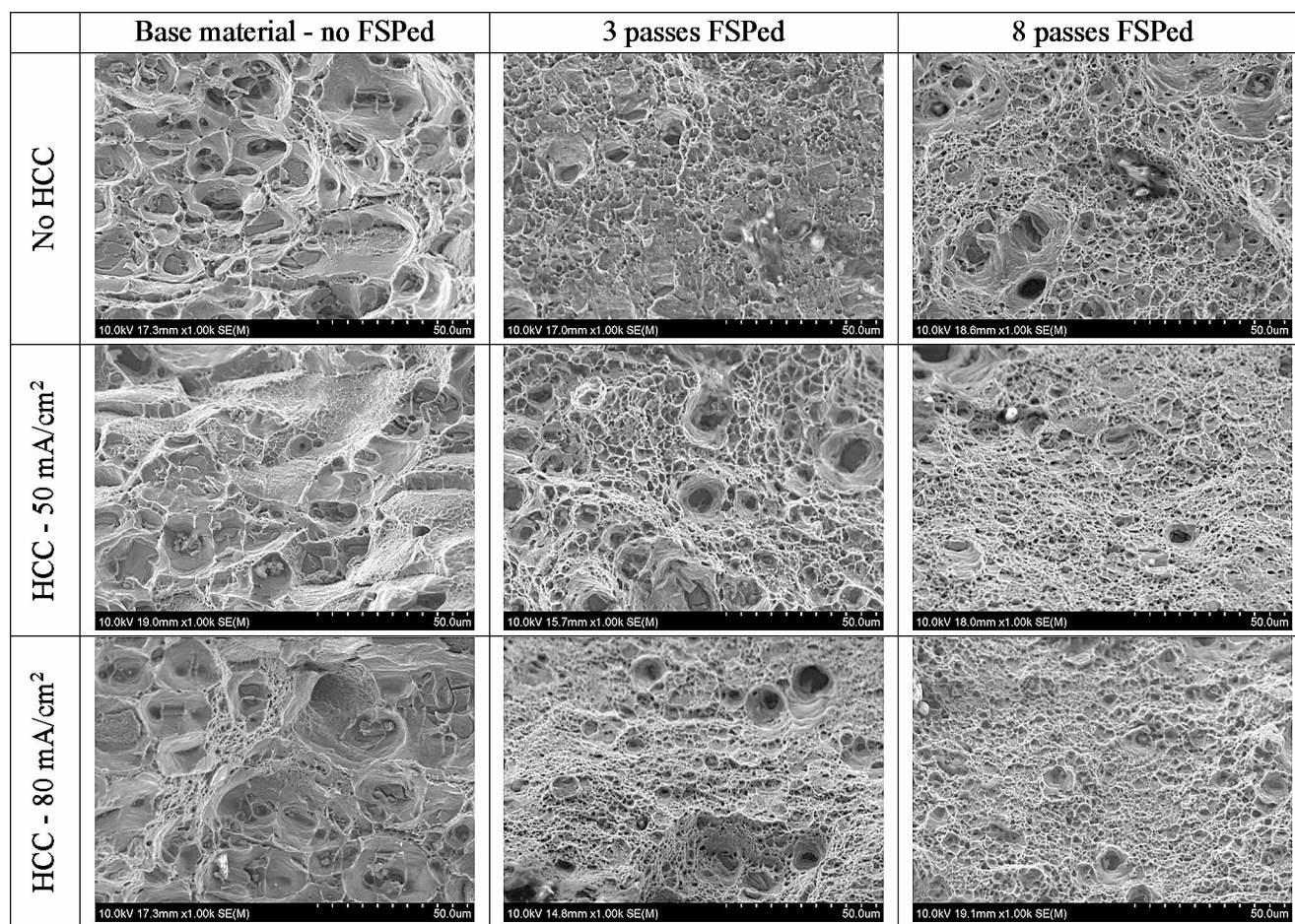


Fig. 11 SEM fracture surface topology micrographs

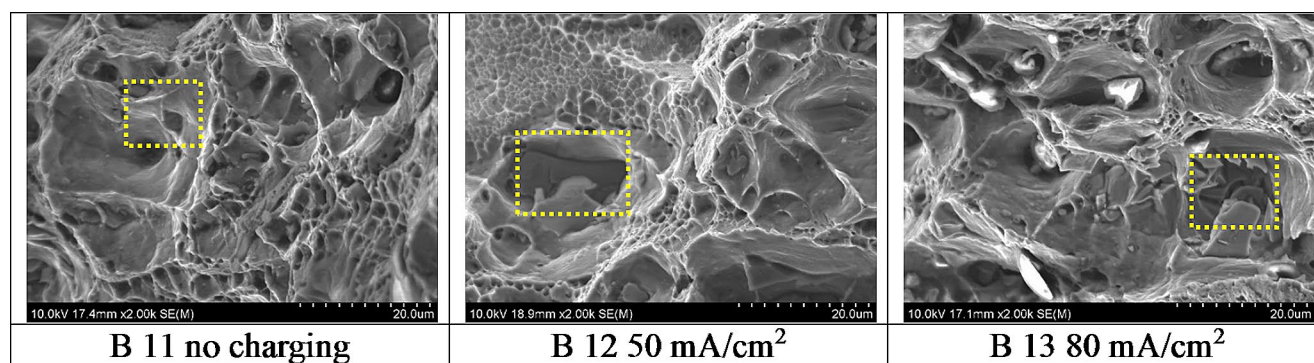


Fig. 12 SEM micrographs revealing fracture surfaces in the base material (non-FSPed) both before and after exposure to HCC. The areas delineated by yellow dashed lines suggest the potential presence of

intermetallic particles, known for their brittleness, which could serve as initiation sites for crack propagation

- The mechanical observations revealed a decrease in yield strength, ultimate tensile strength and microhardness profile accompanied by an increase in energy absorption, as a result of the FSP. These changes in mechanical properties can be attributed to the dissolution and/or coarsening of the hardening precipitates in the stir zone.
- The introduction of hydrogen through HCC significantly reduced energy absorption, yield strength, and UTS in non-FSPed specimens. Charging current density did not appear to have a substantial effect.
- Hydrogen charged specimens with 3 FSP passes presented reduced energy absorption values, but the yield strength and the UTS were not significantly affected.

Notably, a significant energy absorption reduction was introduced at charging current of 80 mA/cm<sup>2</sup>.

- On the other hand, specimens with 8 FSP passes demonstrated increased energy absorption and UTS when subjected to HCC, suggesting the influence of hydrogen-induced microstructural mechanisms.
- The microhardness profiles exhibited a decrease in hardness after the HCC process for the as-received and 3-FSP specimens. However, in correlation with the tensile testing observations, a small increase in microhardness was observed after the HCC process for the 8-FSP specimens. This suggests that the microhardness response is consistent with the mechanical properties, indicating a unique behavior of the 8-FSP specimens compared to the as-received and 3-FSP specimens.
- Microstructural characterization revealed that FSP led to a refined microstructure, with smaller grain sizes and reduced blistering. The microstructure of the stir zone exhibited recrystallization and refinement of second-phase particles.
- The refined microstructure of FSPed specimens displayed enhanced resistance to hydrogen-induced blistering effects, reduced thickness reduction, and smoother surfaces with a significant smaller coverage of the corrosive scale compared to non-FSPed specimens.

The findings of this study shed light on the behavior of hydrogen embrittlement in FSPed aluminum alloys, with a particular focus on the impact of FSP on the resistance to hydrogen-induced blistering effects. The results indicate that the refined microstructures achieved through FSP offer enhanced resistance to hydrogen-related degradation, which is of significant importance in several aspects.

Understanding the behavior of hydrogen embrittlement in FSPed aluminium alloys is of great significance for several reasons. Firstly, FSP is gaining popularity as a surface modification technique for tailoring the mechanical properties of aluminium alloys. However, the influence of FSP on the susceptibility to hydrogen embrittlement needs to be thoroughly investigated to ensure the safe and reliable use of FSPed components in hydrogen-rich environments. Secondly, as the global shift toward greener energy sources gains momentum, hydrogen is increasingly recognized as a promising alternative to conventional fuels. This transition necessitates the development of materials capable of withstanding hydrogen exposure while maintaining their structural integrity. By investigating the hydrogen embrittlement behavior of FSPed aluminum alloys, this study contributes to the understanding of their performance in hydrogen-based applications, such as hydrogen storage, fuel cells, and hydrogen transportation systems.

Thus, the industrial benefits of this research lie in the potential for surface treatment with FSP in components operating in hydrogen-rich environments. This surface treatment has the potential to mitigate hydrogen-related degradation while introducing a decrease in the mechanical strength of the material, but limited to the FSPed surface area and not the whole thickness of the material. By leveraging FSP as a surface treatment technique, it becomes possible to enhance the resistance of materials to hydrogen-related issues, thus paving the way for their utilization in critical applications where both durability and hydrogen compatibility are paramount. Moreover, the insights gained from this study could be of immense value in comprehending how FSW welds respond to hydrogen-rich environments, thereby enriching our understanding of material behavior in such challenging conditions.

**Acknowledgements** Not Applicable.

**Author contributions** - Not Applicable.

**Funding** Funded by the Basic Research Program PEVE 2020 of the National Technical University of Athens. Open access funding provided by HEAL-Link Greece.

**Data Availability** Data will be available on request.

## Declarations

**Ethical approval** Approval was granted to carry out experiments.

**Conflict of interest** It is declared that there are no conflicts of interest under employment, consultancies, stock ownership, honoraria, paid expert testimony, patent applications/registrations and grants or other.

**Open Access** This article is licensed under a Creative Commons Attribution 4.0 International License, which permits use, sharing, adaptation, distribution and reproduction in any medium or format, as long as you give appropriate credit to the original author(s) and the source, provide a link to the Creative Commons licence, and indicate if changes were made. The images or other third party material in this article are included in the article's Creative Commons licence, unless indicated otherwise in a credit line to the material. If material is not included in the article's Creative Commons licence and your intended use is not permitted by statutory regulation or exceeds the permitted use, you will need to obtain permission directly from the copyright holder. To view a copy of this licence, visit <http://creativecommons.org/licenses/by/4.0/>.

## References

1. Z. Ma, Friction stir Processing Technology: a review. *Metall. Mater. Trans. A* **39**, 642–658 (2008). <https://doi.org/10.1007/s11661-007-9459-0>
2. M. Karimi Estahbanati, M. Movahedi, *Met. Mater. Int.* **30**, 284–302 (2024). <https://doi.org/10.1007/s12540-023-01498-4>
3. N. Kumar, R.S. Mishra, N.B. Dahotre, R.E. Brennan, K.J. Doherty, K.C. Cho, Effect of friction stir processing on microstructure

- and mechanical properties of laser-processed Mg4Y3Nd alloy. *Mater. Design* **110**, 663–675 (2016). <https://doi.org/10.1016/j.matdes.2016.08.039>
4. B. Bagheri, M. Abbasi, A. Abdollahzadeh, A.H. Kokabi, A comparative study between friction stir processing and friction stir vibration processing to develop magnesium surface nanocomposites. *Int. J. Miner. Metall. Mater.* **27**, 1133–1146 (2020). <https://doi.org/10.1007/s12613-020-1993-4>
  5. M. Vakili-Azghandi, M. Roknian, J.A. Szpunar, S.M. Mousavizade, Surface modification of pure titanium via friction stir processing: microstructure evolution and dry sliding wear performance. *J. Alloys Compd.* **816**, 152557 (2020). <https://doi.org/10.1016/j.jallcom.2019.152557>
  6. A.K. Srivastava, N. Kumar, A. Saxena, S. Tiwari, Effect of friction stir processing on thermal efficiency and material properties of aluminum alloy AA5083. *Energies* **12**, 1549 (2021). <https://doi.org/10.3390/en12081549>
  7. N. Xu, Y. Xu, B. Zhang, Q. Song, J. Zhao, Y. Bao, Effect of heterogeneous Lamella structure on Mechanical properties of double-pass friction stir processed Cu–30%Zn Alloy. *Met. Mater. Int.* **29**, 3222–3234 (2023). <https://doi.org/10.1007/s12540-023-01448-0>
  8. S. Bharti, N.D. Ghetiya, K.M. Patel, A review on manufacturing surface composites by friction stir processing. *Mater. Manuf. Process.* **36**(2), 135–170 (2021). <https://doi.org/10.1080/10426914.2020.1813897>
  9. S.K. Patel, V.P. Singh, Barnik Saha Roy, & Basil Kuriachen. Recent research progresses in Al-7075 based in-situ surface composite fabrication through friction stir processing: a review. *Mater. Sci. Eng. B* **262**, 114708 (2020). <https://doi.org/10.1016/j.mseb.2020.114708>
  10. S. Olhan, V. Khatkar, B.K. Behera, Impact behavior of long glass fiber-reinforced aluminum metal matrix composite prepared by friction stir processing technique for automotive. *J. Compos. Mater.* **56**(14), 2157–2167 (2022). <https://doi.org/10.1177/00219983221092012>
  11. R. Darji, G. Joshi, V. Badheka, D. Patel, Applications of friction-based processes in Manufacturing, in *Advances in Manufacturing Technology and Management*, ed. by R.M. Singari, P.K. Jain, H. Kumar. Lecture Notes in Mechanical Engineering (Springer, Singapore, 2023). [https://doi.org/10.1007/978-981-16-9523-0\\_27](https://doi.org/10.1007/978-981-16-9523-0_27)
  12. K. Adiga, M.A. Herbert, S.S. Rao, A. Shettigar, Applications of reinforcement particles in the fabrication of Aluminium Metal Matrix composites by Friction stir Processing - A Review. *Manuf. Rev.* **9**, 26 (2022). <https://doi.org/10.1051/mfreview/2022025>
  13. V. Dutta, L. Thakur, B. Singh, A study on the effect of Friction Stir Processing technique for marine applications. *Mater. Today: Proc.* **18**, 5048–5056 (2019). <https://doi.org/10.1016/j.matpr.2019.07.499>
  14. J. Su, J. Wang, R.S. Mishra, R. Xu, J.A. Baumann, Microstructure and mechanical properties of a friction stir processed Ti-6Al-4V alloy. *Mater. Sci. Eng. A* **573**, 67–74 (2013). <https://doi.org/10.1016/j.msea.2013.02.025>
  15. R. Kuroiwa, H. Liu, Y. Aoki, S. Yoon, H. Fujii, G. Murayama, M. Yasuyama, Microstructure control of medium carbon steel joints by low-temperature linear friction welding. *Sci. Technol. Weld. Join.* **25**, 1–9 (2020). <https://doi.org/10.1080/13621718.2019.1600771>
  16. E.B. Moustafa, A. Melaibari, G. Alsuruji, A.M. Khalil, A.O. Mosleh, Tribological and mechanical characteristics of AA5083 alloy reinforced by hybridizing heavy ceramic particles Ta<sub>2</sub>C & VC with light GNP and Al<sub>2</sub>O<sub>3</sub> nanoparticles. *Ceram. Int.* **48**(4), 4710–4721 (2022). <https://doi.org/10.1016/j.ceramint.2021.11.007>
  17. M. Ma, R. Lai, J. Qin, B. Wang, H. Liu, D. Yi, T. Zhai, Achieving exceptionally tensile properties and damage tolerance of 5083 aluminum alloy by friction stir processing assisted by ultrasonic and liquid nitrogen field. *Mater. Sci. Eng. A* **806**, 140824 (2021). <https://doi.org/10.1016/j.msea.2021.140824>
  18. S. Mabuwa, V. Msomi, Fatigue behavior of the multi-pass friction stir processed AA8011-H14 and AA6082-T651 dissimilar joints. *Eng. Fail. Anal.* **118**, 104876 (2020). <https://doi.org/10.1016/j.engfailanal.2020.104876>
  19. A.R. Eivani, M. Mehdizade, S. Chabok, J. Zhou, Applying multi-pass friction stir processing to refine the microstructure and enhance the strength, ductility, and corrosion resistance of WE43 magnesium alloy. *J. Mater. Res. Technol.* **12**, 1946–1957 (2021). <https://doi.org/10.1016/j.jmrt.2021.03.021>
  20. V. Sharma, U. Prakash, B.V.M. Kumar, Surface composites by friction stir processing: a review. *J. Mater. Process. Technol.* **224**, 117–134 (2015). <https://doi.org/10.1016/j.jmatprotec.2015.04.019>
  21. P.B. Berbon, W.H. Bingel, R.S. Mishra, C.C. Bampton, M.W. Mahoney, Friction stir processing: a tool to homogenize nanocomposite aluminum alloys. *Scripta Mater.* **44**, 61–66 (2001). [https://doi.org/10.1016/S1359-6462\(00\)00578-9](https://doi.org/10.1016/S1359-6462(00)00578-9)
  22. M.J. Starink, A. Deschamps, S.C. Wang, The strength of friction stir welded and friction stir processed aluminum alloys. *Scripta Mater.* **58**(5), 377–382 (2008). <https://doi.org/10.1016/j.scriptamat.2007.09.061>
  23. E.B. Moustafa, A.O. Mosleh, Effect of (Ti–B) modifier elements and FSP on 5052 aluminum alloy. *J. Alloys Compd.* **823**, 153745 (2020). <https://doi.org/10.1016/j.jallcom.2020.153745>
  24. J. Su, T.W. Nelson, C.J. Sterling, Microstructure evolution during FSW/FSP of high-strength aluminum alloys. *Mater. Sci. Eng. A* **405**, 277–286 (2005). <https://doi.org/10.1016/j.msea.2005.06.009>
  25. M.S. Prabhu, A.E. Perumal, S. Arulvel, R.F. Issac, Friction and wear measurements of friction stir-processed aluminum alloy 6082/CaCO<sub>3</sub> composite. *Measurement* **142**, 10–20 (2019). <https://doi.org/10.1016/j.measurement.2019.04.061>
  26. C.J. AnandhaKumar, Gopi S., S. Shashi Kumar, D.G. Mohan, Mechanical, metallurgical, and Tribological properties of Friction stir processed aluminum Alloy 6061 Hybrid Surface composites. *Surf. Topogr. Metrol. Prop.* **9**, 045019 (2021). <https://doi.org/10.1088/2051-672X/ac3120>
  27. C. Örnek, M. Mansoor, A. Larsson, F. Zhang, G.S. Harlow, R. Kroll, F. Carlà, H. Hussain, B. Derin, U. Kivisäkk, D.L. Engelberg, E. Lundgren, J. Pan, The causation of hydrogen embrittlement of duplex stainless steel: phase instability of the austenite phase and ductile-to-brittle transition of the ferrite phase – synergy between experiments and modeling. *Corros. Sci.* **217**, 111140 (2023). <https://doi.org/10.1016/j.corsci.2023.111140>
  28. P.C. Okonkwo, E.M. Barhoumi, I.B. Belgacem, I.B. Mansir, M. Aliyu, W. Emori, P.C. Uzoma, W.H. Beitelmal, E. Akyüz, A.B. Radwan, R.A. Shakoob, A focused review of the hydrogen storage tank embrittlement mechanism process. *Int. J. Hydrogen Energy* **48**, 12935–12948 (2023). <https://doi.org/10.1016/j.ijhydene.2022.12.252>
  29. Y. Li, Q. Wang, H. Zhang, H. Zhu, M. Wang, H. Wang, Role of solute atoms and vacancy in hydrogen embrittlement mechanism of aluminum: A first-principles study. *Int. J. Hydrogen Energy* **48**, 4516–4528 (2023). <https://doi.org/10.1016/j.ijhydene.2022.10.257>
  30. A. Del-Pozo, J.C. Villalobos, A. Bedolla-Jacuinde, H.J. Vergara-Hernández, O. Vázquez-Gómez, B. Campillo, Low hydrogen pressure effect over microhardness and impact toughness of an experimental X-120 microalloyed steel. *Int. J. Press. Vessels Pip.* **203**, 104946 (2023). <https://doi.org/10.1016/j.ijpvp.2023.104946>
  31. C. Cui, R. Ma, E. Martínez-Pañeda, A generalised, multi-phase-field theory for dissolution-driven stress corrosion cracking and hydrogen embrittlement. *J. Mech. Phys. Solids* **166**, 104951 (2022). <https://doi.org/10.1016/j.jmps.2022.104951>



32. Y. Hong, C. Zhou, S. Wagner, S. Schlabach, A. Pundt, L. Zhang, J. Zheng, Strain-induced twins and martensite: effects on hydrogen embrittlement of selective laser melted (SLM) 316 L stainless steel. *Corros. Sci.* **208**, 110669 (2022). <https://doi.org/10.1016/j.corsci.2022.110669>
33. M.R. Louthan, G.R. Caskey, J.A. Donovan, D.E. Rawl, Hydrogen embrittlement of metals. *Mater. Sci. Eng.* **10**, 357–368 (1972). [https://doi.org/10.1016/0025-5416\(72\)90109-7](https://doi.org/10.1016/0025-5416(72)90109-7)
34. J. Song, W. Curtin, Atomic mechanism and prediction of hydrogen embrittlement in iron. *Nat. Mater.* **12**, 145–151 (2013). <https://doi.org/10.1038/nmat3479>
35. A.R. Troiano, The role of hydrogen and other interstitials in the mechanical behavior of metals. *Trans. ASM.* **52**, 54–80 (1960)
36. I.M.A. Ghermaoui, A. Oudriss, A. Metsue, R. Milet, K. Madani, X. Feaugas, Multiscale analysis of hydrogen-induced softening in f.c.c. nickel single crystals oriented for multiple-slips: elastic screening effect. *Sci. Rep.* **9**, 13042 (2019). <https://doi.org/10.1038/s41598-019-49420-6>
37. M. Safyari, M. Moshtaghi, S. Kuramoto, On the role of traps in the microstructural control of environmental hydrogen embrittlement of a 7xxx series aluminum alloy. *Journal of Alloys and Compounds*, Volume 855, Part 1, 157300 (2021). <https://doi.org/10.1016/j.jallcom.2020.157300>
38. M. Safyari, M. Moshtaghi, S. Kuramoto, Effect of strain rate on environmental hydrogen embrittlement susceptibility of a severely cold-rolled Al–Cu alloy. *Vacuum.* **172**, 109057 (2020). <https://doi.org/10.1016/j.vacuum.2019.109057>
39. N.D. Alexopoulos, Z. Velonaki, C.I. Stergiou, S.K. Kourkoulis, The effect of artificial ageing heat treatments on the corrosion-induced hydrogen embrittlement of 2024 (Al–Cu) aluminum alloy. *Corros. Sci.* **102**, 413–424 (2016). <https://doi.org/10.1016/j.corsci.2015.10.034>
40. S. Dey, I. Chattoraj, Interaction of strain rate and hydrogen input on the embrittlement of 7075 T6 aluminum alloy. *Mater. Sci. Eng. A* **661**, 168–178 (2016). <https://doi.org/10.1016/j.msea.2016.03.010>
41. S.L. Chou, W.T. Tsai, Hydrogen embrittlement of duplex stainless steel in concentrated sodium chloride solution. *Mater. Chem. Phys.* **60**, 137–142 (1999). [https://doi.org/10.1016/S0254-0584\(99\)00077-2](https://doi.org/10.1016/S0254-0584(99)00077-2)
42. H. Najam, M. Koyama, B. Bal, E. Akiyama, Tsuzaki., strain rate and hydrogen effects on crack growth from a notch in a Fe-high-Mn steel containing 1.1 wt% solute carbon. *Int. J. Hydrog. Energy.* **45**, 1125–1139 (2020). <https://doi.org/10.1016/j.ijhydene.2019.10.227>
43. I.G. Papantoniou, P. Karmiris-Obratański, B. Leszczyńska-Madej, D. Manolakos, The effect of friction stir processing on the hydrogen susceptibility of AA5083 specimens after hydrogen cathodic charging. *Int. J. Adv. Manuf. Technol.* **125**, 4399–4413 (2023). <https://doi.org/10.1007/s00170-023-10971-8>
44. M. Jula, R. Dehmlaei, K. Ranjbar, Softening, hardening, and Precipitation Evolution of the AA6082-T651 heat-affected Zone caused by thermal cycles during and after welding. *Met. Mater. Int.* **29**, 3664–3678 (2023). <https://doi.org/10.1007/s12540-023-01470-2>
45. P. Cavaliere, A. De Santis, F. Panella, A. Squillace, Effect of welding parameters on mechanical and microstructural properties of dissimilar AA6082–AA2024 joints produced by friction stir welding. *Mater. Design* **30**, 609–616 (2009). <https://doi.org/10.1016/j.matdes.2008.05.044>
46. D. Pérez Escobar, C. Miñambres, L. Duprez, K. Verbeken, M. Verhaege, Internal and surface damage of multiphase steels and pure iron after electrochemical hydrogen charging. *Corros. Sci.* **53**, 3166–3176 (2011). <https://doi.org/10.1016/j.corsci.2011.05.060>
47. P.M.G.P. Moreira, T. Santos, S.M.O. Tavares, V. Richter-Trummer, P. Vilaça, P.M.S.T. de Castro, *Mater. Design* **30**, 180–187 (2009). <https://doi.org/10.1016/j.matdes.2008.04.042>
48. E. Cerri, P. Leo, Influence of high-temperature thermal treatment on grain stability and mechanical properties of medium-strength aluminium alloy friction stir welds. *J. Mater. Process. Technol.* **213**, 75–83 (2013). <https://doi.org/10.1016/j.jmatprotec.2012.09.001>
49. S.Y. Kondrat'ev, Y.N. Morozova, Y.A. Golubev, C. Hantelmann, A.A. Naumov, V.G. Mikhailov, Microstructure and Mechanical properties of Welds of Al–mg–Si alloys after different modes of impulse friction stir Welding. *Met. Sci. Heat. Treat.* **59**, 697–702 (2018). <https://doi.org/10.1007/s11041-018-0213-6>
50. B. Milkereit, N. Wanderka, C. Schick, O. Kessler, Continuous cooling precipitation diagrams of Al–Mg–Si alloys. *Mater. Sci. Eng. A* **550**, 87–96 (2012). <https://doi.org/10.1016/j.msea.2012.04.033>
51. E.A. El-Danaf, M.M. El-Rayes, Microstructure and mechanical properties of friction stir welded 6082 AA in as welded and post weld heat-treated conditions. *Mater. Design* **46**, 561–572 (2013). (1980–2015). <https://doi.org/10.1016/j.matdes.2012.10.047>
52. W. Zhang, H. He, C. Xu, W. Yu, L. Li, Precipitates Dissolution, Phase Transformation, and Re-precipitation-induced Hardness Variation in 6082-T6 Alloy during MIG Welding and subsequent baking. *JOM* **71**, 2711–2720 (2019). <https://doi.org/10.1007/s11837-019-03375-1>
53. M.M. El-Rayes, E.A. El-Danaf, The influence of multi-pass friction stir processing on the microstructural and mechanical properties of Aluminum Alloy 6082. *J. Mater. Process. Technol.* **212**, 1157–1168 (2012). <https://doi.org/10.1016/j.jmatprotec.2011.12.017>
54. E. Lunarska, A. Mikeladze, Effect of second phase particles on hydrogen embrittlement of iron alloys. *International Journal of Hydrogen Energy*, Volume 22, Issues 2–3, 131–139 (1997). [https://doi.org/10.1016/S0360-3199\(96\)00164-4](https://doi.org/10.1016/S0360-3199(96)00164-4)
55. E. Lunarska, O. Chernyaeva, Effect of precipitates on hydrogen transport and hydrogen embrittlement of aluminum alloys. *Mater. Sci.* **40**, 399–407 (2004). <https://doi.org/10.1007/PL00022004>
56. Q. Dai, Y. Deng, H. Jiang, J. Tang, J. Chen, Hot tensile deformation behaviors and a phenomenological AA5083 aluminum alloy fracture damage model. *Mater. Sci. Eng. A* **766**, 138325 (2019). <https://doi.org/10.1016/j.msea.2019.138325>

**Publisher's Note** Springer Nature remains neutral with regard to jurisdictional claims in published maps and institutional affiliations.